

Enrico Rinaldi

Process and Energy Department,
Delft University of Technology,
Leeghwaterstraat 39,
Delft 2628 CB, The Netherlands
e-mail: e.rinaldi@tudelft.nl

Rene Pecnik¹

Assistant Professor
Process and Energy Department,
Delft University of Technology,
Leeghwaterstraat 39,
Delft 2628 CB, The Netherlands
e-mail: r.pecnik@tudelft.nl

Piero Colonna

Professor
Aerodynamics, Wind Energy,
Flight Performance and Propulsion Department,
Delft University of Technology,
Kluyverweg 1,
Delft 2629 HS, The Netherlands
e-mail: p.colonna@tudelft.nl

Computational Fluid Dynamic Simulation of a Supercritical CO₂ Compressor Performance Map

The performance map of a radial compressor operating with supercritical CO₂ is computed by means of three-dimensional steady state Reynolds-averaged Navier–Stokes simulations. The geometry investigated is part of a 250 kW prototype which was tested at Sandia National Laboratories (SNL). An in-house fluid dynamic solver is coupled with a lookup table algorithm to evaluate the fluid properties. Tables are generated using a multiparameter equation of state, which ensures high accuracy in the fluid characterization. The compressor map is calculated considering three different rotational speeds (45 krpm, 50 krpm, and 55 krpm). For each speed-line, several mass flow rates are simulated. Numerical results are compared to experimental data from SNL to prove the potential of the methodology. [DOI: 10.1115/1.4029121]

1 Introduction

The idea of using supercritical carbon dioxide (sCO₂) as the working fluid of closed loop Brayton cycle turbines for energy conversion was first studied in the late sixties by Angelino [1] and Feher [2]. The main advantage of this cycle configuration is the much higher conversion efficiency reachable at moderate maximum cycle temperatures, compared to competing technologies. This is possible because of the small work needed to compress the fluid close to its vapor–liquid critical point and of the use of a high degree of regeneration. A further advantage of sCO₂ power cycle turbines is the high power density, which leads to compact general assemblies, due to the high operating fluid densities and pressures.

These studies were recently resumed by the scientific community because of the high potential of using sCO₂ cycles in next-generation nuclear reactors [3–6] or to exploit low/medium temperature renewable energy sources such as solar radiation [7–10]. This interest led to the realization of several proof-of-concept test loop facilities, as for example the one operating at Sandia National Laboratories (SNL) [11,12].

Despite the fervid activity, no commercial sCO₂ power unit is currently operational. Among the challenges that need to be faced to bring this technology to the market, we list the development of robust control strategies, the realization of cost effective compact heat exchangers, and the improvement of the turbomachinery performance. While significant progress has been made in the design of turbomachinery operating with fluids behaving as ideal gases, only recently the interest was shifted to nonconventional machines operating with dense vapors or supercritical fluids [13–18]. Although simple one dimensional or surrogate models are commonly used for preliminary designs, only accurate fluid dynamic simulations can provide important insights on the flow field that can be used to improve the machine aerodynamics and therefore its performance. Difficulties in the simulation and analysis of

flows evolving close to the fluid vapor–liquid critical point arise from the highly nonlinear variations of the fluid thermophysical properties in this region.

This paper presents a methodology for the computational fluid dynamic (CFD) simulation of the compressible flow of sCO₂ in a radial compressor. The component analyzed is part of a 250 kW prototype investigated experimentally by Wright et al. [11]. A Reynolds-averaged Navier–Stokes (RANS) solver [19] was coupled to a multiparameter equation of state model to evaluate the thermophysical properties of the fluid [20,21]. A brief overview of the real gas CFD code is provided in the following, together with a description of the compressor geometry and computational mesh. Three-dimensional steady state simulations were performed using a mixing-plane to treat the rotor–diffuser interface at three different rotational speeds of the impeller (45 krpm, 50 krpm, and 55 krpm) and for several mass flow rates. Finally, numerical results are compared to experiments and discussed.

2 CFD Solver for Dense Vapor and Supercritical Fluid Flows

The compressible RANS equations were solved using the CFD code developed by Pecnik et al. [19]. The solver is based on a cell-centered finite volume formulation on unstructured arbitrary polyhedral meshes. It uses a subdomain decomposition through the freely available package Parmetis and the message passing interface as the parallel infrastructure. The equations are discretized in the conservative form

$$\frac{\partial}{\partial t} \int_{\Omega} U d\Omega + \int_{\partial\Omega} (\mathbf{F}_c(\mathbf{U}) - \mathbf{F}_d(\mathbf{U})) dA = \int_{\Omega} \mathbf{S} d\Omega \quad (1)$$

$\mathbf{U} = \mathbf{U}(\mathbf{x}, t) = (\rho, \mathbf{m}, E^t)^T$ represents the conserved variables vector, with ρ being the density, $\mathbf{m} = \rho\mathbf{v}$ as the Cartesian momentum, and $E^t = \rho(e + |\mathbf{v}|^2/2)$ as the total internal energy. $\mathbf{F}_c(\mathbf{U})$ and $\mathbf{F}_d(\mathbf{U})$ are the convective and diffusive fluxes, \mathbf{S} is the source term, and Ω and $\partial\Omega$ are the physical domain of interest and its boundary.

The fluxes and source term vectors are expressed for a rotating noninertial reference frame as

¹Corresponding author.

Contributed by the Turbomachinery Committee of ASME for publication in the JOURNAL OF ENGINEERING FOR GAS TURBINES AND POWER. Manuscript received October 6, 2014; final manuscript received October 22, 2014; published online December 17, 2014. Editor: David Wisler.

$$\mathbf{F}_c(\mathbf{U}) = \begin{pmatrix} \mathbf{n} \cdot \rho(\mathbf{v} - \mathbf{v}^m) \\ \rho \mathbf{v}(\mathbf{n} \cdot (\mathbf{v} - \mathbf{v}^m)) + P \mathbf{n} \\ (E^t + P)((\mathbf{v} - \mathbf{v}^m) \cdot \mathbf{n}) + P(\mathbf{v}^m \cdot \mathbf{n}) \end{pmatrix},$$

$$\mathbf{F}_d(\mathbf{U}) = \begin{pmatrix} 0 \\ \mathbf{n} \cdot \Pi \\ \mathbf{v} \cdot (\mathbf{n} \cdot \Pi) + \mathbf{n} \cdot (\lambda \nabla T) \end{pmatrix}, \quad \mathbf{S}(\mathbf{U}) = \begin{pmatrix} 0 \\ -\rho(\boldsymbol{\omega} \times \mathbf{v}) \\ 0 \end{pmatrix} \quad (2)$$

where $\boldsymbol{\omega}$ denotes the angular velocity of the rotating noninertial reference frame, $\mathbf{v}^m = \boldsymbol{\omega} \times \mathbf{r}$, P is the pressure, Π is the stress tensor, λ is the thermal conductivity, T is the temperature, and \mathbf{n} is the outward pointing unit vector normal to the surface.

The convective fluxes are discretized using the AUSM⁺ approximate Riemann solver proposed by Liou [22]. Second order accuracy is achieved using a suitable interpolation scheme (least-squares gradient) to reconstruct the state (ρ , \mathbf{v} , P) at each cell face. The slope limiter proposed by Venkatakrishnan [23] and later modified by one of the authors [19] is used to reduce the discrete gradients to guarantee the monotonicity of the reconstructed variable at the face center. In order to ensure thermodynamic consistency of the reconstructed state, the fluid state is evaluated at the faces using the interpolated density and pressure.

The diffusive fluxes discretization needs an accurate and efficient evaluation of the gradients at the cell faces. Following Kim et al. [24], the velocity and temperature gradients at the faces are calculated as

$$\nabla \phi|_f \cdot \mathbf{n}_f = \frac{\phi_A - \phi_B}{|\mathbf{x}_A - \mathbf{x}_B|} \alpha_f + \frac{1}{2} (\nabla \phi|_A + \nabla \phi|_B) \cdot (\mathbf{n}_f - \alpha_f \mathbf{s}_f) \quad (3)$$

where ϕ is a generic variable, A and B are the two cell centers sharing the face f , and $\alpha = \mathbf{s} \cdot \mathbf{n}$.

The set of equations is closed using the $k-\omega$ shear stress transport model of Menter [25], which represents a standard choice in turbomachinery flows computations.

In order to increase the robustness of the simulations, first order accuracy was used for the convective fluxes, while the diffusive fluxes were discretized using a second order scheme.

Equations are implicitly integrated in time using the backward Euler scheme to allow for the choice of large time steps. A newly introduced implicit formulation of AUSM⁺ is adopted, while the diffusive fluxes Jacobian is expressed in the form suggested by Pulliam and Steger [26]. The Jacobians of the convective and diffusive fluxes expressed for a fluid governed by a complex equation of state are taken from Rinaldi et al. [27]. The large sparse system resulting from the fluxes linearization is solved using PETSc [28].

2.1 Thermophysical Model. In order to accurately estimate the thermodynamic and transport properties of the supercritical fluid, a reference model based on the multiparameter equation of state of Span and Wagner [20] is used. The viscosity is computed based on the work of Fenghour et al. [29], while the other transport properties are based on Vesovic et al. [30]. A lookup table interpolation method recently developed by the authors couples the solver to the evaluation of fluid properties in order to greatly reduce the computational time [27]. The property table is obtained with an in-house library [31], which links to a well-known thermodynamic property program [21] for the evaluation of primary properties, while it relies on its own routines for the evaluation of secondary or derived properties (e.g., the pressure and temperature derivatives needed for the implicit time integration). The tabulated region is split into separate single phase and two-phase property tables to avoid large interpolation errors which would occur for states lying close to the vapor–liquid saturation lines, because



Fig. 1 Impeller and diffuser geometry [11]

some properties (e.g., the speed of sound or pressure derivatives) are discontinuous across the boundary separating the single phase and vapor–liquid equilibrium (VLE) states. The number of nodes of the tables used in the simulations was chosen in order to guarantee that the maximum interpolation error in the whole tabulated region is below 0.1%.

2.2 Boundary Conditions. Constant total conditions and turbulence properties were specified at the compressor inlet, see Table 2, while a constant static pressure was set at the diffuser outlet. A no-slip boundary condition was applied at the walls, which were modeled as adiabatic. The mixing-plane approach [32] was applied to treat the interface between rotor and diffuser.

3 Geometry and Computational Mesh

The investigated case is the single stage radial compressor operating in the proof-of-concept test loop facility at SNL and is shown in Fig. 1. The rotor consists of six main blades and six splitter blades, while the diffuser is made of 17 wedge shaped blades. The geometrical specifications are taken from Wright et al. [11] and summarized in Table 1. They were used to generate the three-dimensional geometry by means of a commercial software [33].

An in-house hybrid mesh generator was used to generate a flexible and high quality computational grid. The adopted software employs a geometry transformation tailored to turbomachinery geometries, which reduces the complexity of the mesh generation from three to two dimensions. The original geometry is discretized into several constant span level surfaces in the physical space (x , y , z). The frame of reference is then changed to (M, ϕ, s) , with M being the normalized meridional length, ϕ being the azimuthal angle, and s being the normalized span. The surfaces can be therefore meshed using two-dimensional grid generation schemes in the transformed space. The planes are finally transformed back to the physical space, and a node interpolation in the spanwise direction is performed in order to fill the whole three-

Table 1 Main compressor dimensions [11]

Inlet shroud radius	9.3720 mm
Inlet hub radius	2.5375 mm
Exit blade height	1.7120 mm
Exit blade radius	18.6817 mm
Blade thickness	0.762 mm
Tip clearance	0.254 mm
Radial rotor/diffuser blades gap	0.3 mm
Inlet blade angle at tip	50 deg
Exit blade back sweep angle	−50 deg
Exit vaned diffuser angle	71.5 deg
Diffuser blade divergence angle	13.17 deg

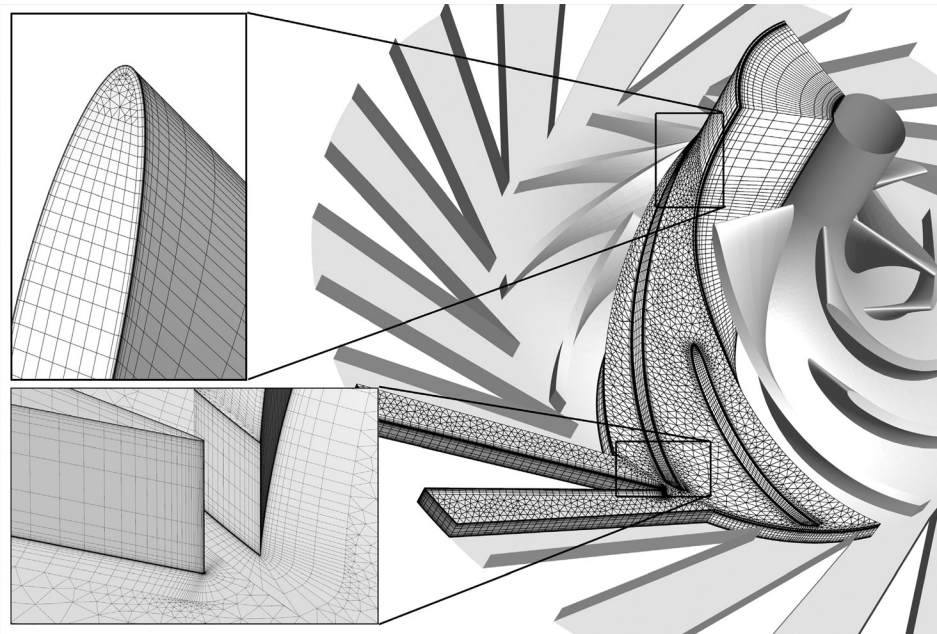


Fig. 2 Three-dimensional view of the computational mesh used to model the rotor and the diffuser vanes. The grid counts approximately 8×10^5 cells, which are clustered at the walls to ensure $y^+ \approx 1$. Hexahedral cells were used for the blades boundary layers and at the inlet of the rotor, while wedge cells were placed elsewhere. Detailed views are shown for the surface mesh of the rotor main blade, diffuser wedge, and the interface between rotor and diffuser.

dimensional domain. In the present study, five equally spaced span level surfaces were employed.

An O-type structured mesh was used around the blades, and the elements were clustered at the walls to have the correct resolution of the boundary layers. The normal-to-wall velocity profile was fully resolved using a sufficiently fine grid, $y^+ \approx 1$ at the walls. An unstructured triangulation [34] was used for the remaining part of the domain. In order to have the same mesh topology in terms of connectivity and number of nodes on the five planes (needed for the interpolation in the spanwise direction), the unstructured triangulation was performed at the hub only ($s = 0$), and morphed and smoothed (using a Laplacian scheme) on the other levels to match the new boundaries. The impeller and the tip clearance gap were meshed separately using 39 and 19 elements in the spanwise direction, respectively. The discretization of the diffuser was straightforward due to the simplicity of the geometry. At the leading edge of the diffuser blade, a small curvature was introduced to remove numerical problems due to the sharp corner.

The periodicity of the geometry and the steady flow assumption allow to simulate only one passage of the rotor and one of the diffuser using about 6.5×10^5 and 1.5×10^5 elements, respectively. The mesh resolution was refined with respect to the previous studies [18] in order to ensure more accurate results. Figure 2 shows the modeled compressor geometry and the computational grid, with detailed views of the main blade leading and trailing edge and of the interface region.

4 Discussion of the CFD Model and of the Available Experimental Data

4.1 Numerical Model. A critical aspect of the fluid dynamic modeling of the problem under investigation is the treatment of fluid condensation. Previous studies [18,35,36] indicated that the fluid thermodynamic state falls in the VLE region near the leading edge of the main compressor blade. Since the main goal of this investigation is the estimation of the typical performance parameters with engineering accuracy, the adoption of the single-fluid model allows to avoid a considerable increase of complexity.

Therefore, the homogeneous mixture approximation was used for the thermodynamic states lying inside the VLE region. Properties were averaged based on the vapor quality, and metastable states were not considered.

This modeling choice is further justified by the lack of accurate nucleation models close to the critical point and of experimental data against which the extended fluid flow model could be validated. Moreover, the small density differences between the liquid and vapor phases close to the critical point suggest that the influence of this modeling approximation on the results is marginal, given the small dimension of the regions where the thermodynamic state falls inside the dome. In addition to that, Baltadjev et al. [36] and Lettieri et al. [37] shown that in practice the short residence time of the flow prevents condensation from taking place (their results were however obtained for operating conditions farther from the critical point than the ones studied in this paper).

A general limitation of RANS modeling, especially for supercritical flows, is the reliability of turbulence models to accurately mimic the effects of turbulence. Most of the models were developed and calibrated for incompressible flows of gases obeying to the ideal gas law and for simple geometries. For a comprehensive assessment, the reader is referred to the work of He et al. [38]. One of the issues is the definition of the effective thermal conductivity, which is commonly modeled as the sum of molecular λ and turbulent thermal conductivity λ_{tur} , $\lambda_{\text{eff}} = \lambda + \lambda_{\text{tur}}$, with

Table 2 Inlet boundary conditions [11]. $Tu = \sqrt{2/3k}/U$ is the inlet turbulence intensity, with k being the turbulent kinetic energy and U being the average velocity at the inlet. $Re_T = \sqrt{k}L\rho/\mu$ is the inlet turbulent Reynolds number. Tu and Re_T are used to calculate the inlet values of turbulent kinetic energy and specific dissipation ω used by the turbulence model.

P_{tot} (bar)	T_{tot} (°C)	Tu (%)	Re_T
76.9	32.8	5	100

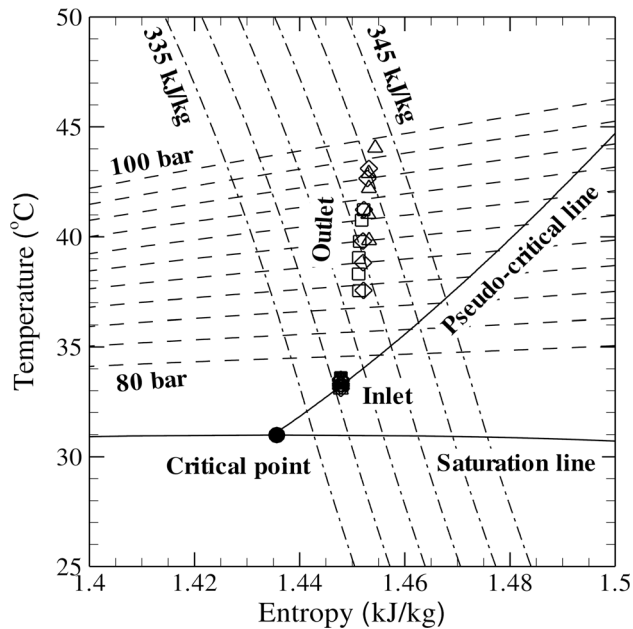


Fig. 3 Average inlet and outlet states. Symbols correspond to 45 krpm (squares), 50 krpm (diamonds), and 55 krpm (triangles).

$\lambda_{\text{tur}} = c_p \mu_{\text{tur}} / \text{Pr}_{\text{tur}}$, and μ_{tur} and Pr_{tur} being the turbulent viscosity and turbulent Prandtl number, respectively. While the turbulent Prandtl number can be assumed constant for an ideal gas flow, it varies significantly for a supercritical flow [39,40]. Furthermore, the value of the fluid specific heat capacity c_p is not defined in the homogeneous mixture model, if the thermodynamic state is in the VLE region. For these reasons, λ_{tur} was not included in the heat transfer term in the energy equation. This modification to the equations is not expected to affect significantly the results since strong temperature gradients are not present in the flow field and the assumption of adiabatic walls was used.

4.2 Experimental Data. The inlet conditions were taken from Wright et al. [11]; however, the values applied in the simulations may differ from the ones measured during the experimental campaign. In fact, the report does not specify the exact location of the sensors and whether the measured inlet quantities are total or static. In this work, constant total conditions were assumed and the reported values were interpreted as such.

It is worth mentioning that applying constant static conditions instead of total conditions can result in significant changes in the inlet fluid properties for states close to the critical point. This is due to the strong nonlinearities and the large density, which leads to large differences between static and total conditions even for small velocities. For example, for the condition with the largest mass flow rate considered in this work, $\Delta P / P_{\text{tot}} = ((1/2)\rho_{\text{in}} U_{\text{in}}^2) / P_{\text{tot}} \approx 2.5\%$. Accordingly, the transport properties change as $\Delta \mu / \mu_{\text{in}} \approx 1.7\%$, $\Delta c_p / c_{p,\text{in}} \approx 41\%$, $\Delta \lambda / \lambda_{\text{in}} \approx 14\%$.

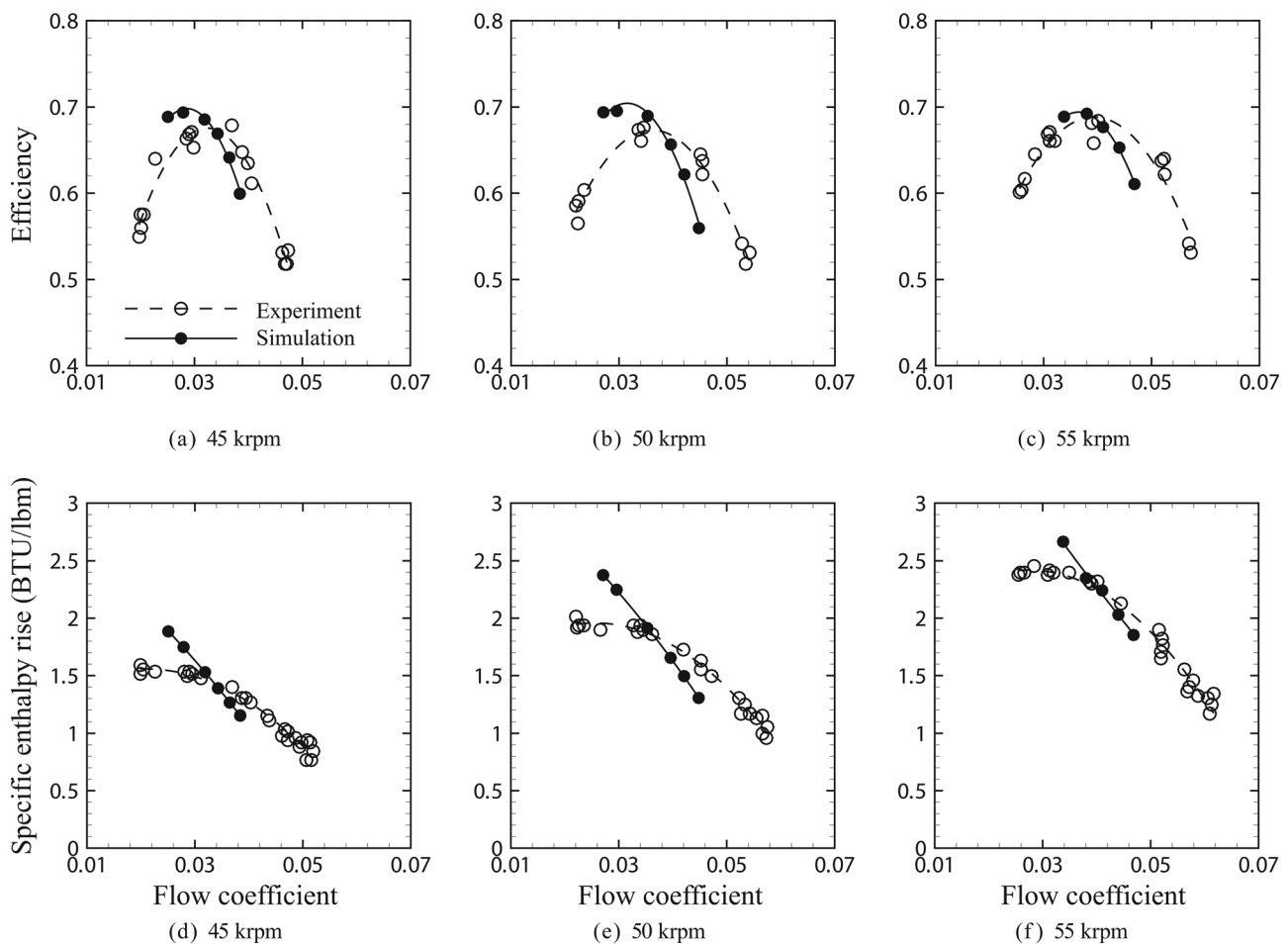
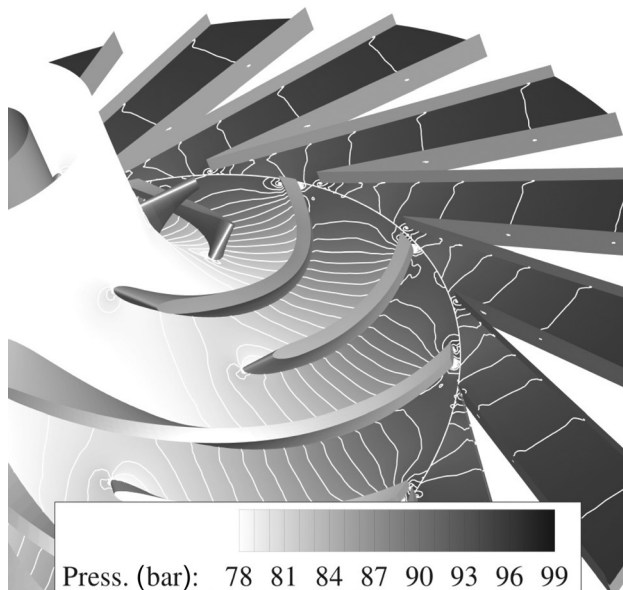
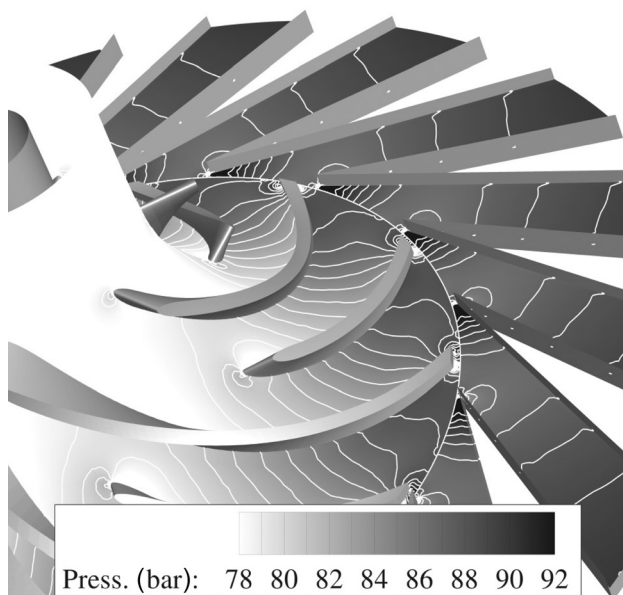


Fig. 4 Compressor performance map



(a) $\phi = 0.038$ and $\eta = 69.2\%$



(b) $\phi = 0.0468$ and $\eta = 61\%$

Fig. 5 Contours of pressure at 50% of the span and 55 krpm

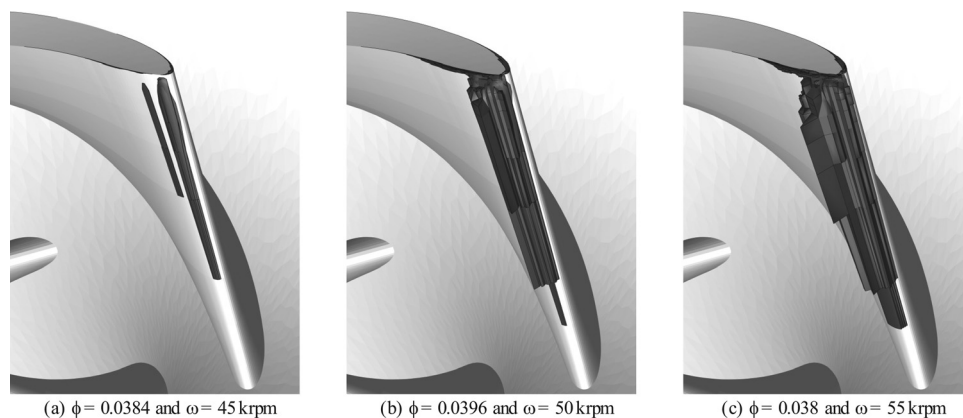


Fig. 6 Main blade leading edge: control volumes where the thermodynamic state is in the VLE region

In addition, the measured inlet conditions are given within ranges of pressure $P = [77, 81.39]$ bar and temperature $T = [304.3, 307]$ K. The uncertainty on pressure and temperature translates into a large density range $\rho = [345, 690]$ kg/m³.

Furthermore, the compressor map measured experimentally in Ref. [11] is also affected by uncertainties related to measurement equipment, flow leakage, windage losses, etc., which are not taken into account in the CFD simulations.

5 Results

The compressor map was calculated by performing steady state simulations at three different rotational speeds, namely 45 krpm, 50 krpm, and 55 krpm. The inlet conditions are reported in Table 2.

Figure 3 shows the averaged inlet and outlet states of all simulations in the $T-s$ diagram. Isopressure and isoenthalpy lines in the range of the outlet values are also shown. Note that all the compression processes cross the pseudocritical line for the conditions considered, which is the locus of thermodynamic states where the specific heat at constant pressure peaks and where transition between liquid-like and vapor-like behavior occurs.

The compressor performance is assessed in Fig. 4 in terms of isentropic efficiency $\eta = (h_{out,s} - h_{in}) / (h_{out} - h_{in})$ and specific enthalpy rise. Numerical results are compared with experimental data from Wright et al. [11]. The calculated efficiency curves are reasonably close to the experimental data, showing a slight shift toward low flow coefficients. The difference between numerical values and experiments is within an arguably acceptable range, given the limitations discussed in Sec. 4. The specific enthalpy rise obtained from the simulations shows a nearly linear dependence on the flow coefficient. Therefore, the presented simulations do not capture the compressor surge at low mass flow rates and high pressure ratios (which is clearly visible in the experimental data). The order of accuracy of the convective fluxes discretization is expected to play an important role in the representation of the loss mechanisms (e.g., flow separations), and as a consequence in the performance prediction. The fact that no back-flow or recirculation is allowed at the outlet of the diffuser can also influence the results when the operating conditions are close to surge.

Pressure contours are depicted in Fig. 5 at half of the span height for two mass flow rates and at a rotational speed of 55 krpm. The distribution is smooth due to the small value of the relative Mach number in the rotor, which reaches about $M = 0.5$ at the interface location. Figure 5(a) corresponds to the calculated maximum efficiency for the considered speed line, whereby the velocity angle at the inlet of the diffuser is well aligned with the diffuser blade, and the diffuser recovers pressure efficiently. A small stagnation region can be identified by the high pressure at the leading edge of the blade. As the mass flow increases, see

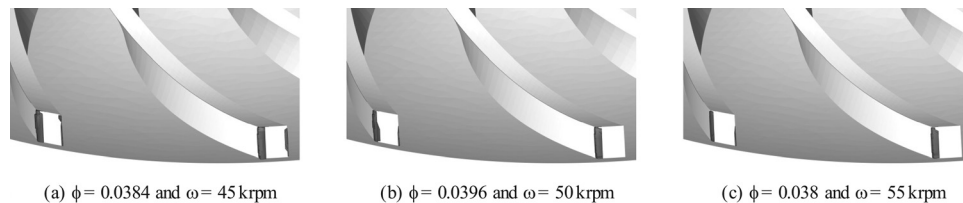


Fig. 7 Main and splitter blade trailing edge: control volumes where the thermodynamic state is in the VLE region

Fig. 5(b) which corresponds to the minimum efficiency of the 55 krpm speed line, the flow at the outlet of the rotor has a larger radial component. For this reason, it impinges on one side of the diffuser blade, leading to a large stagnation region which affects the overall pressure recovery in the diffuser vane. Moreover, the flow accelerates around the blade leading edge determining a small low pressure region.

Finally, it is possible to identify regions of the domain where the calculated thermodynamic states are located inside the VLE region, therefore where there is the possibility for CO₂ to condense. As already mentioned, this phenomenon has not been modeled in the presented simulations. Nevertheless, qualitative conclusions can still be drawn from the analysis of the computed flow fields. Figures 6 and 7 present the predicted two-phase flow regions for the three considered rotational speeds, at nearly constant flow coefficients. At the leading edge of the compressor main blade, shown in Fig. 6, the surface which delimits the single phase and the two-phase region becomes larger for increasing rotational speeds, and is stretched in the direction of the hub. This was not observed at the leading edge of the splitter blade, where the fluid state is in the vapor single phase for each simulated condition. Given the high value of the design rotational speed, namely 75 krpm, the predicted two-phase regions are expected to increase significantly. Because of the proximity to the critical point of the inlet state, conditions for condensation can be met and consequently the modeling of two-phase flow can be important in order to predict the flow accurately.

A similar phenomenon occurs at the trailing edge of both blades, as depicted in Fig. 7, where the flow acceleration around the sharp corners determines a large drop in the static pressure, see Fig. 5. However, the dependence on the rotational speed is weaker and appears reversed. The largest region is observed for the lowest rotational speed.

For high mass flows, a two-phase flow region is predicted at the diffuser leading edge also. This can be explained referring to Fig. 5(b). When the inlet flow angle is not aligned with the diffuser blade, the large acceleration around the sharp leading edge is such that the thermodynamic state falls below the saturation lines.

6 Conclusions

The performance map of a radial compressor operating with supercritical CO₂ was calculated by means of three-dimensional steady state simulations. The in-house computational tool is formed by a parallel RANS solver for unstructured grids obtaining fluid thermophysical properties thanks to a lookup table interpolation method. Thermophysical fluid property tables are generated with an in-house program implementing state-of-the-art models, allowing for accurate predictions even close to the fluid critical point and in the VLE region.

Numerical results were compared to experimental data over a range of mass flow rates and for three values of the impeller rotational speed. The qualitative and quantitative predictions of the compressor isentropic efficiency were satisfactory, however showing a shift of the optimal operating condition toward low values of

the flow coefficient. The specific enthalpy rise of the fluid predicted with simulations depends linearly on the mass flow, differently from values measured from experiments. Furthermore, the compressor surge could not be simulated due to the limitations of the model.

The difference between experimental and numerical results was discussed by addressing the limitations of the adopted models and those related to the experimental data.

The computed flow fields showed a smooth variation of fluid properties and allowed to gain insights on the compressor performance degradation for high mass flow rates. Simulations also highlighted the possibility of CO₂ condensation in some regions of the domain and allowed the study of the dependence of their extent on the impeller rotational speed. The volume of calculated thermodynamic states lying in the VLE region at the leading edge of the impellers is predicted to grow for increasing rotational speeds. A similar phenomenon with a weaker dependence on the rotational speed was observed at the trailing edge of both the main and the splitter blades, however, with a reversed dependence on the rotational speed if compared to the main blade leading edge.

In conclusion, the potential of using three-dimensional CFD simulations for the improvement of the aerodynamic design of nonconventional turbomachinery, such as the ones operating with supercritical fluids, was demonstrated. Although models can still be improved to a large extent, they can provide reasonable performance predictions and valuable information about the flow field that can be used in the design process.

Acknowledgment

The development of the Navier–Stokes solver has been supported by the (U.S.) Department of Energy (DOE) (National Nuclear Security Administration) under Award No. NA28614.

References

- [1] Angelino, G., 1968, "Carbon Dioxide Condensation Cycles for Power Production," *ASME J. Eng. Power*, **90**(3), pp. 287–295.
- [2] Feher, E. G., 1968, "The Supercritical Thermodynamic Power Cycle," *Energy Convers.*, **8**(2), pp. 85–90.
- [3] Dostal, V., Hejzlar, P., and Driscoll, M. J., 2006, "High-Performance Supercritical Carbon Dioxide Cycle for Next-Generation Nuclear Reactors," *Nucl. Technol.*, **154**(3), pp. 265–282.
- [4] Dostal, V., Hejzlar, P., and Driscoll, M. J., 2006, "The Supercritical Carbon Dioxide Power Cycle: Comparison to Other Advanced Power Cycles," *Nucl. Technol.*, **154**(3), pp. 283–301.
- [5] Ishiyama, S., Muto, Y., Kato, Y., Nishio, S., Hayashi, T., and Nomoto, Y., 2008, "Study of Steam, Helium and Supercritical CO₂ Turbine Power Generations in Prototype Fusion Power Reactor," *Prog. Nucl. Energy*, **50**(2–6), pp. 325–332.
- [6] Kim, Y. M., Kim, C. G., and Favrat, D., 2012, "Transcritical or Supercritical CO₂ Cycles Using Both Low- and High-Temperature Heat Sources," *Energy*, **43**(1), pp. 402–415.
- [7] Yamaguchi, H., Sawada, N., Suzuki, H., Ueda, H., and Zhang, X.-R., 2010, "Preliminary Study on a Solar Water Heater Using Supercritical Carbon Dioxide as Working Fluid," *ASME J. Sol. Energy*, **132**(1), p. 011010.
- [8] Garg, P., Kumar, P., and Srinivasan, K., 2013, "Supercritical Carbon Dioxide Brayton Cycle for Concentrated Solar Power," *J. Supercrit. Fluids*, **76**, pp. 54–60.

- [9] Iverson, B. D., Conboy, T. M., Pasch, J. J., and Kruienga, A. M., 2013, "Supercritical CO₂ Brayton Cycles for Solar-Thermal Energy," *Appl. Energy*, **111**, pp. 957–970.
- [10] Turchi, C. S., Ma, Z., Neises, T. W., and Wagner, M. J., 2013, "Thermodynamic Study of Advanced Supercritical Carbon Dioxide Power Cycles for Concentrating Solar Power Systems," *ASME J. Sol. Energy*, **135**(4), p. 041007.
- [11] Wright, S. A., Radel, R. F., Vernon, M. E., Rochau, G. E., and Pickard, P. S., 2010, "Operation and Analysis of a Supercritical CO₂ Brayton Cycle," Sandia National Laboratories, Livermore, CA, Sandia Report No. SAND2010-0171.
- [12] Conboy, T., Wright, S., Pasch, J., Fleming, D., Rochau, G., and Fuller, R., 2012, "Performance Characteristics of an Operating Supercritical CO₂ Brayton Cycle," *ASME J. Eng. Gas Turbines Power*, **134**(11), p. 111703.
- [13] Boncinelli, P., Rubecchini, F., Arnone, A., Cecconi, M., and Cortese, C., 2004, "Real Gas Effects in Turbomachinery Flows: A Computational Fluid Dynamics Model for Fast Computations," *ASME J. Turbomach.*, **126**(2), pp. 268–276.
- [14] Colonna, P., Harinck, J., Rebay, S., and Guardone, A., 2008, "Real-Gas Effects in Organic Rankine Cycle Turbine Nozzles," *J. Propul. Power*, **24**(2), pp. 282–294.
- [15] Harinck, J., Guardone, A., and Colonna, P., 2009, "The Influence of Molecular Complexity on Expanding Flows of Ideal and Dense Gases," *Phys. Fluids*, **21**(8), p. 086101.
- [16] Harinck, J., Colonna, P., Guardone, A., and Rebay, S., 2010, "Influence of Thermodynamic Models in Two-Dimensional Flow Simulations of Turboexpanders," *ASME J. Turbomach.*, **132**(1), p. 011001.
- [17] Congedo, P. M., Corre, C., and Cinnella, P., 2011, "Numerical Investigation of Dense-Gas Effects in Turbomachinery," *Comput. Fluids*, **49**(1), pp. 290–301.
- [18] Pecnik, R., Rinaldi, E., and Colonna, P., 2012, "Computational Fluid Dynamics of a Radial Compressor Operating With Supercritical CO₂," *ASME J. Eng. Gas Turbines Power*, **134**(12), p. 122301.
- [19] Pecnik, R., Terrapon, V. E., Ham, F., Iaccarino, G., and Pitsch, H., 2012, "Reynolds-Averaged Navier–Stokes Simulations of the HyShot II Scramjet," *AIAA J.*, **50**(8), pp. 1717–1732.
- [20] Span, R., and Wagner, W., 2003, "Equations of State for Technical Applications. I. Simultaneously Optimized Functional Forms for Nonpolar and Polar Fluids," *Int. J. Thermophys.*, **24**(1), pp. 1–39.
- [21] Lemmon, E. W., McLinden, M. O., and Huber, M. L., 2002, "NIST Standard Reference Database 23: Reference Fluid Thermodynamic and Transport Properties-REFPROP, Version 8.0," National Institute of Standards and Technology, Standard Reference Data Program, Gaithersburg, MD.
- [22] Liou, M.-S., 1996, "A Sequel to AUSM: AUSM⁺," *J. Comput. Phys.*, **129**(2), pp. 364–382.
- [23] Venkatakrishnan, V., 1995, "Convergence to Steady State Solutions of the Euler Equations on Unstructured Grids With Limiters," *J. Comput. Phys.*, **118**(1), pp. 120–130.
- [24] Kim, S.-E., Makarov, B., and Caraeni, D., 2003, "A Multi-Dimensional Linear Reconstruction Scheme for Arbitrary Unstructured Grids," *AIAA* Paper No. 2003-3990.
- [25] Menter, F. R., 1994, "Two-Equation Eddy-Viscosity Turbulence Models for Engineering Applications," *AIAA J.*, **32**(8), pp. 1598–1605.
- [26] Pulliam, T. H., and Steger, J. L., 1985, "Recent Improvements in Efficiency, Accuracy, and Convergence for Implicit Approximate Factorization Algorithms," *AIAA* Paper No. 85-0360.
- [27] Rinaldi, E., Pecnik, R., and Colonna, P., 2014, "Exact Jacobians for Implicit Navier–Stokes Simulations of Equilibrium Real Gas Flows," *J. Comput. Phys.*, **270**, pp. 459–477.
- [28] Satish, B., Buschelman, K., Eijkhout, V., Gropp, W. D., Kaushik, D., Knepley, M. G., McInnes, L. C., Smith, B. F., and Zhang, H., 2009, "PETSc: Portable, Extensible Toolkit for Scientific Computation," <http://www.mcs.anl.gov/petsc>
- [29] Fenghour, A., Wakeham, W. A., and Vesovic, V., 1998, "The Viscosity of Carbon Dioxide," *J. Phys. Chem. Ref. Data*, **27**(1), pp. 31–39.
- [30] Vesovic, V., Wakeham, W. A., Olchowy, G. A., Sengers, J. V., Watson, J. T. R., and Millat, J., 1990, "The Transport Properties of Carbon Dioxide," *J. Phys. Chem. Ref. Data*, **19**(3), pp. 763–808.
- [31] Colonna, P., van der Stelt, T. P., and Guardone, A., 2012, "FluidProp (Version 3.0): A Program for the Estimation of Thermophysical Properties of Fluids," Asimptote, Delft, The Netherlands, <http://www.fluidprop.com/>
- [32] Denton, J. D., 1992, "The Calculation of Three-Dimensional Viscous Through Multistage Turbomachines," *ASME J. Turbomach.*, **114**(1), pp. 18–26.
- [33] ANSYS, 2009, ANSYS BLADEGEN, Release 13.0 User's Guide, ANSYS, Inc., Canonsburg, PA.
- [34] Shewchuk, J. R., 2002, "Delaunay Refinement Algorithms for Triangular Mesh Generation," *Comp. Geom. Theory Appl.*, **22**(1–3), pp. 21–74.
- [35] Rinaldi, E., Pecnik, R., and Colonna, P., 2013, "Steady State CFD Investigation of a Radial Compressor Operating With Supercritical CO₂," *ASME* Paper No. GT2013-94580.
- [36] Baltadjiev, N., Lettieri, C., and Spakovszky, Z., 2014, "An Investigation of Real Gas Effects in Supercritical CO₂ Centrifugal Compressors," *ASME* Paper No. GT2014-26180.
- [37] Lettieri, C., Yang, D., and Spakovszky, Z., 2014, "An Investigation of Condensation Effects in Supercritical Carbon Dioxide Compressors," 4th International Symposium—Supercritical CO₂ Power Cycles, Pittsburgh, PA, Sept. 9–10.
- [38] He, S., Kim, W. S., and Bae, J. H., 2008, "Assessment of Performance of Turbulence Models in Predicting Supercritical Pressure Heat Transfer in a Vertical Tube," *Int. J. Heat Mass Transfer*, **51**(19–20), pp. 4659–4675.
- [39] Yoo, J. Y., 2013, "The Turbulent Flows of Supercritical Fluids With Heat Transfer," *Annu. Rev. Fluid Mech.*, **45**(1), pp. 495–525.
- [40] Nemati, H., Patel, A., Boersma, B. J., and Pecnik, R., 2013, "Direct Numerical Simulation of Turbulent Flow With Supercritical Fluid in a Heated Pipe," International Symposium on Turbulence and Shear Flow Phenomena (TSFP-8), Poitiers, France, Aug. 28–30.